batteries

MDPI

Article

A Millimeter-Resolution Operando Thermal Image of Prismatic Li-Ion Batteries Using a Distributed Optical Fiber Sensor

Zhen Guo [1,*], Mina Abedi Varnosfaderani [2], Calum Briggs [1], Erdogan Guk [1] and James Marco [1]

[1] Warwick Manufacturing Group (WMG), University of Warwick, Coventry CV4 7AL, UK; calum.briggs@warwick.ac.uk (C.B.); erdogan.guk@warwick.ac.uk (E.G.); james.marco@warwick.ac.uk (J.M.)
[2] Jaguar Land Rover, Banbury Road Gaydon, Lighthorne Heath, Warwick CV35 0RR, UK; mabediv1@jaguarlandrover.com
* Correspondence: zhen.guo@warwick.ac.uk

Abstract: With the demand for energy gravimetric and volumetric density in electrical vehicles, lithium-ion batteries are undergoing a trend toward larger formats, along with maximized cell-to-pack efficiency. Current battery thermal management systems and battery modeling, relying on point measurement (thermocouples/thermistors), face challenges in providing comprehensive characterization for larger batteries and extensive monitoring across the pack. Here, we proposed a novel Rayleigh-scattering-based distributed optical fiber sensor to deliver thermal images of a large prismatic cell. Using an optical fiber of 1 mm diameter wrapped around the cell, the optical sensor delivered over 400 unique measurement locations at 3 mm spatial resolution. During a 1.0 C charge, the optical-measured maximum temperature difference was 8.2 °C, while point-like thermocouples, located at the cell front surface and rear surface center, only had a 0.8 °C maximum temperature difference. Moreover, the all-surface-covered optical sensor identified hotspot generation around the vicinity of the tabs, highlighting the essential role of tabs. The maximum temperature on the negative current tab reached 113.9 °C during a 1.5 C discharge, while the hottest spot on the cell surface was only 52.1 °C. This was further validated by the operando thermal image in both the time domain and the spatial domain, facilitating a detailed analysis of the thermal-behavior-like heat generation on the current tabs, transmission through the surface, and dissipation to the cell bottom.

Keywords: Li-ion battery; LIB; thermal gradient; distributed optical fiber sensor; optical frequency domain reflectometer

check for updates

Received: 13 November 2024
Revised: 16 December 2024
Accepted: 23 December 2024
Published: 8 January 2025

Citation: Guo, Z.; Varnosfaderani, M.A.; Briggs, C.; Guk, E.; Marco, J. A Millimeter-Resolution Operando Thermal Image of Prismatic Li-Ion Batteries Using a Distributed Optical Fiber Sensor. *Batteries* **2025**, *11*, 19. https://doi.org/10.3390/batteries11010019

Copyright: © 2025 by the authors. Licensee MDPI, Basel, Switzerland. This article is an open access article distributed under the terms and conditions of the Creative Commons Attribution (CC BY) license (https://creativecommons.org/licenses/by/4.0/).

1. Introduction

Due to the excellent energy density, rechargeable lithium-ion batteries (LIBs) have been widely used as energy storage devices in portable electronics, electric vehicles, power grids, and aerospace applications. The widespread adoption of Li-ion batteries underscores the increasing importance of battery reliability and lifetime performance to these sectors. However, improper operation can result in the sudden release of stored chemical energy, leading to fires or explosions [1]. Honeywell Safety and Productivity Solutions reported a concerning trend, with 239 electric vehicle fires recorded in the United Kingdom between July 2022 and June 2023—an 83% increase compared to the previous year. High-profile incidents, such as electric vehicle fires [2,3], airplane issues [4,5], and mobile phone explosions [6,7], serve as constant reminders that safety must remain a top priority in the battery industry.

Temperature plays a critical role in determining the charging and discharging performance, as well as the energy storage capacity, of lithium-ion batteries (LIBs) [8–10]. An uneven temperature distribution within a battery module or pack can lead to electrically unbalanced cells, compromising overall performance and safety. To mitigate these challenges, battery thermal management systems (BTMSs) are commonly implemented to maintain battery temperatures within the optimal operating range and minimize temperature variations between cells [11–14]. For Li-ion batteries, the recommended operating temperature range is between 25 °C and 40 °C, with a maximum allowable temperature variation among cells of less than 5 °C [15].

Traditional temperature monitoring methods that rely on point-like sensors, such as thermocouples and thermistors, face significant challenges as the trend toward larger cell formats—from 18,650 and 21,700 cylindrical cells to 4680 cylindrical cells and larger pouch/prismatic designs—thermal behavior becomes increasingly complex, necessitating more sophisticated monitoring for accurate battery and pack modeling [16]. Point-like sensors fall short in providing sufficient data to characterize thermal gradients, especially in large-format cells and modules/packs. For instance, studies show that the radial temperature distribution within cylindrical 18,650 cells is non-uniform. Understanding these gradients is crucial for optimizing cooling strategies and validating electrochemical-thermal coupled battery models [17]. Similarly, in pouch cells, the perpendicular thermal gradient has been shown to induce faster degradation compared to in-plane gradients [18]. Notably, the in-plane temperature difference on an A5-sized pouch cell is measured to be up to 307% higher than values obtained using thermocouples [19]. Moreover, internal sensing provides more accurate monitoring and deeper insights into battery operation than surface measurements alone [20,21]. These challenges underscore the need for advanced sensing solutions that offer large-scale coverage, ease of integration, and mechanical robustness to address the evolving demands of modern battery systems.

Scattering-based distributed optical fiber sensors (DOFSs) have emerged as a promising technology for cell instrumentation and characterization [22–24]. Unlike point-like sensors, such as Fabry–Perot (F-P) interferometers [25,26], traditional interferometers [27–29], and semi-distributed fiber Bragg grating (FBG) sensors [30–32], a DOFS provides distributed measurement capabilities. Among DOFS technologies, phase-sensitive optical time domain reflectometers (φ-OTDRs) are widely used due to their high accuracy and sensitivity [33–35]. However, their resolution is constrained by the pulse duration and digitizer limitations. In contrast, optical frequency domain reflectometry (OFDR), enabled by wavelength-tunable laser sources, offers significant advantages, including millimeter-to-sub-millimeter spatial resolution and fine measurement accuracy [36,37]. These features make OFDR an ideal method for advanced battery thermal monitoring. To further enhance this approach, we developed an OFDR interrogator with the ultimate resolution by effectively mitigating laser nonlinear noise and random wavelength drifts [38–40]. This advancement positions OFDR as a highly effective solution for addressing the thermal monitoring challenges in modern battery systems.

In this paper, we used such a distributed optical fiber sensor with 3 mm spatial resolution to instrument a large-format prismatic cell to deliver an operando thermal image covering the complete battery surface. The instrumented optical sensor provided over 400 unique measurement locations using just one 1 mm diameter fiber, covering four cell surfaces, positive/negative current tabs, and a vent. Comparisons were made between the thermal characterization measured by the distributed optical sensors and the point-like thermocouples. The optical-measured thermal difference was 1025% higher than the difference measured by thermocouples. The spatial temperature distribution on the prismatic cell revealed non-uniform heat generation during the cell operation, with the hottest spots

consistently appearing near the vicinity of the current tabs. Furthermore, the operando thermal image was presented to reveal the detailed thermal behavior of the prismatic cell. We believe that the operando thermal image with millimeter-level resolution provides a potential methodology for the further development of cell/module/pack optimization, battery modeling, and battery thermal management systems.

2. Theory and Methods

2.1. Distributed Optical Fiber Sensor

Distributed optical sensing, using an optical frequency domain reflectometer (OFDR), operates as illustrated in Figure 1a. A wavelength-swept light is generated by a tunable laser source (TLS) and introduced into the optical fiber. Due to the inherent non-uniformity in the refractive index of the fiber, Rayleigh backscattering occurs randomly along its length. When the temperature of a specific fiber segment, Δz, changes, the Rayleigh scattering spectrum peaks shift correspondingly.

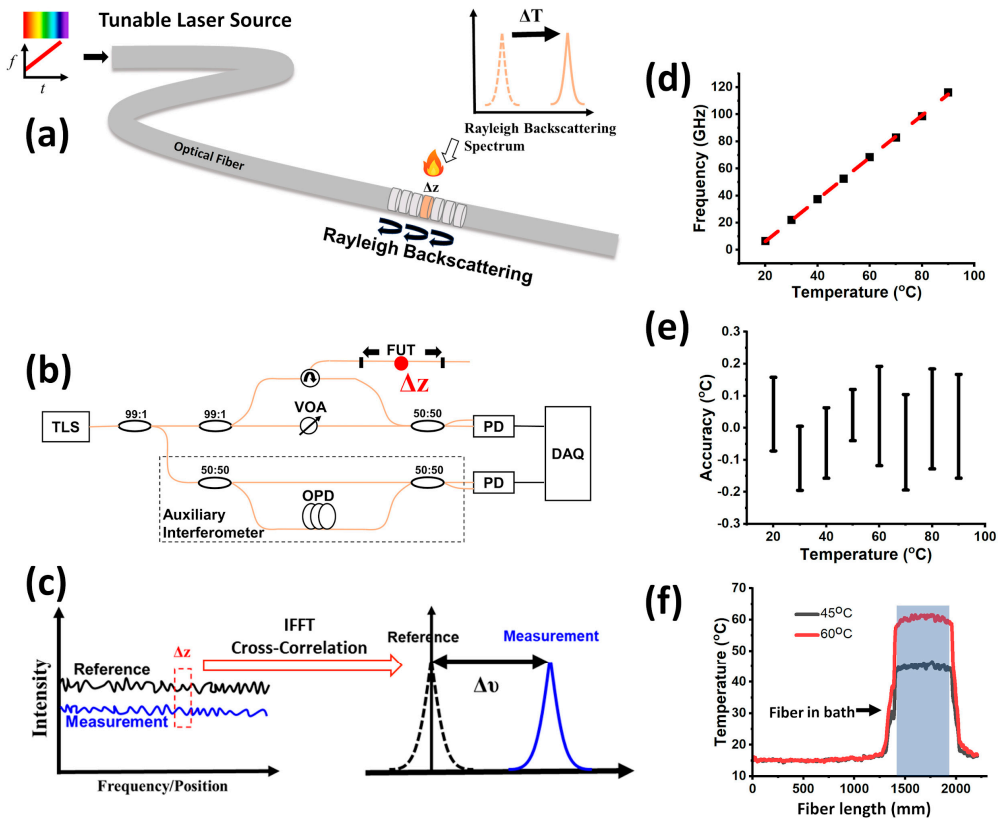

Figure 1. (**a**) Schematic illustration of distributed measurement based on OFDR. (**b**) Experimental setup [39]. (**c**) Demodulation process [39]. (**d**) Temperature calibration between the applied temperature and the measured frequency shift. (**e**) Measurement accuracy under 3 mm resolution. (**f**) Distributed optical measurements with segments of optical fiber in the water bath.

The experimental configuration of the optical frequency domain reflectometer (OFDR) is depicted in Figure 1b. It consists of a tunable laser source and two interferometers. The fiber under test (FUT) is placed in one arm of the interferometer, while the other arm incorporates a variable optical attenuator (VOA) to control the interference intensity. Rayleigh-backscattered light from the FUT is routed via an optical circulator and captured by a photodetector (PD). During the wavelength sweep with speed γ, the interference

signal between a specific position z in the fiber under test and the local oscillator can be expressed as [37]:

$$I(t) = E(z)^2 cos\left[2\pi\left(v_0\tau_z + \gamma\tau_z t - \frac{1}{2}\gamma\tau_z^2\right) + \varphi_n(t,\tau_z)\right] \quad (1)$$

where τ_z is the time delay between the position z in the FUT and the reference arm. The term $\gamma\tau_z t$ is the beating frequency with position z along the fiber. Consequently, the signals captured by the photodetector, denoted as $\sum_z I(t)$, represent the summation of various frequency components originating from each segment of the fiber under test.

OFDR demodulation is crucial in determining the performance of distributed measurement. This process, detailed in our previous study [37], involves three main steps: fast Fourier transform, slidewindow, and cross-correlation, as depicted in Figure 1c. The frequency shift, Δv, of each fiber segment, Δz, is then calculated to represent the applied temperature variation [41]:

$$\frac{\Delta v}{v} = -K_T \Delta T \quad (2)$$

where υ is the mean optical frequency and K_T is the optical fiber thermal coefficient.

However, intrinsic noise in OFDR systems, such as nonlinear tuning noise and random wavelength tuning variations, must be addressed to achieve the ultimate resolution. To mitigate these challenges, equal-frequency resampling and wavelength range calibration techniques have been proposed, effectively suppressing nonlinear sweep noise and enabling high-resolution distributed measurements [39]. For detailed thermal analysis, a spatial resolution of 3 mm has been established. The tunable laser source used in the system is the Santec TSL-550, featuring an output power of 9.0 dBm and a wavelength sweep range of 1540–1550 nm. To further address nonlinear sweep noise, an auxiliary interferometer is incorporated into the setup. The optical path delay (OPD) length of this auxiliary interferometer is set at 191 m, ensuring accurate calibration and enhanced system performance.

The temperature calibration of optical measurement is depicted in Figure 1d. A segment of optical fiber is positioned within a thermal chamber and secured to a metal plate. A reference thermocouple (RS PRO Type K) is placed adjacent to the fiber. The calculated OFDR frequency shift exhibits a linear relationship with the temperature variation, demonstrating a coefficient of correlation of 0.985. The sensitivity of optical measurement is 1.55 GHz/°C. The measurement accuracy is further discussed in Figure 1e. It should be noted that accuracy is influenced by the resolution during distributed measurement. For the fine thermal monitoring required in subsequent battery characterization, a 3 mm measurement resolution was selected. Given that the wavelength sweep range is 10 nm, the theoretical resolution was calculated to be 82.2 µm ($\Delta z = c/2n\upsilon_sweep$). Therefore, the length of the slidewindow was 36 for 3 mm resolution. The optical measurement accuracy was limited to ±0.2 °C under 3 mm resolution. OFDR optimization between resolution and accuracy has been discussed in [39]. The distributed temperature measurements were validated in Figure 1f. A fiber segment spanning from 1411 to 1956 mm was immersed in a water bath with an ambient temperature of 15 °C. With 3 mm resolution, there were 181 measurement locations delivered by the distributed optical sensor. The distributed optical measurement agreed with the temperature variation in the water bath.

2.2. Prismatic Cell Instrumentation and Experimental Setup

The candidate LIB used in this paper was a prismatic cell with an 86 Ah nominal energy capacity, as shown in Figure 2a. The cathode comprised nickel, cobalt, and manganese (NCM) impaired with a Gr-doped graphite anode. The cell operated within a voltage

range of 2.8 V to 4.2 V. The dimension was 39.5 mm × 148 mm × 100 mm. Compared to the cylindrical 21,700/4680 battery, the prismatic cell offers increased capacity and a larger format. Thus, more heat generation and thermal gradient can be expected during the operation.

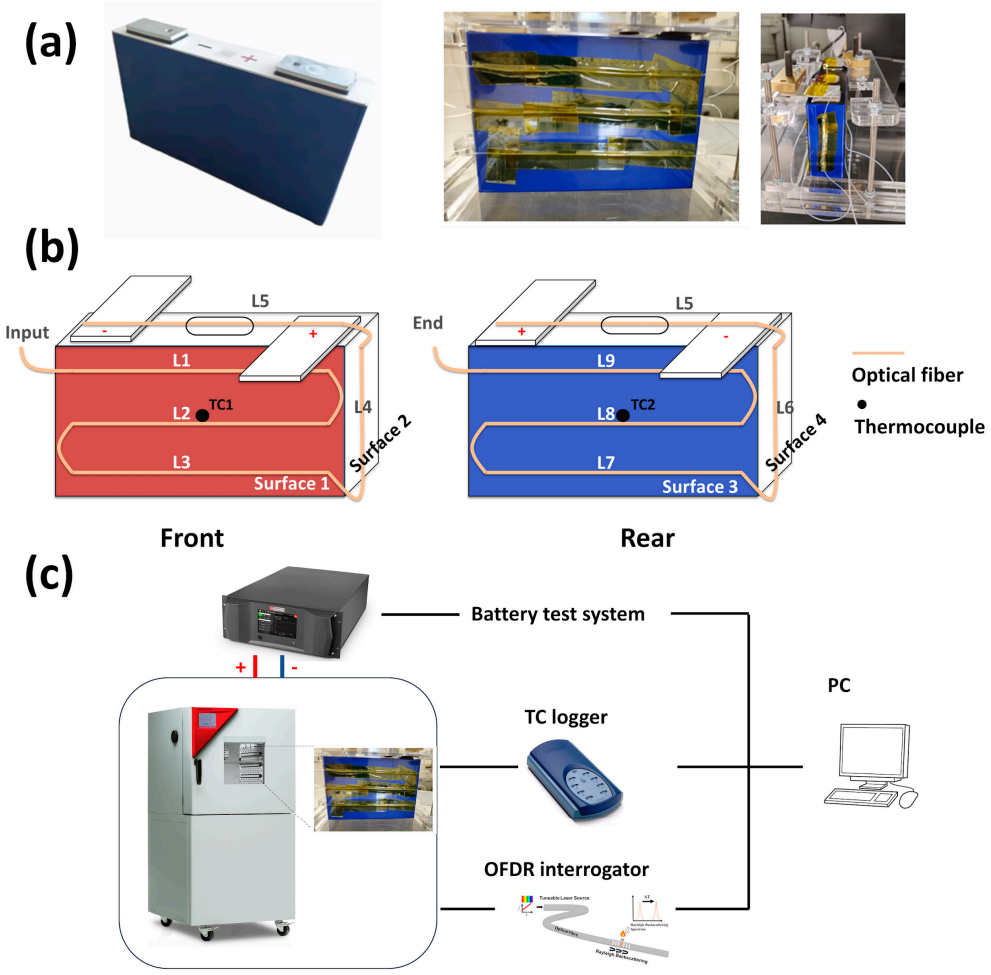

Figure 2. (**a**) Left—pristine prismatic cell; right—optical fiber instrumented cell. (**b**) Optical fiber layout of the prismatic cell. (**c**) Experimental setup of the instrumented cell.

A single 5-meter-long optical fiber sensor was wrapped around the prismatic cell for the whole-surface thermal monitoring, as illustrated in Figure 2a. It should be noted that during charge/discharge, the battery surface would experience deformation/swelling due to the internal chemical reaction or gas generation. This could affect the accuracy of the instrumented optical temperature sensor, as the bare optical fiber is sensitive to both temperature and strain [42,43]. Therefore, the optical sensor was encapsulated within a 1 mm PTFE tube for strain insulation. The optical fiber sensor was fixed on the battery surface using the Kapton tape. The deployment of the optical fiber sensor is depicted in Figure 2b. L1 was horizontally instrumented on the front surface, 25 mm below the top of the cell. L2 was at the middle height, while L3 was positioned 25 mm above the bottom. Both side surfaces were also instrumented with the optical fiber sensor: L4 was placed on the surface near the positive tab, and L6 was near the negative tab. As the optical fiber was made of silica and coated with acrylate, it could be directly attached to the metal surface of the current tabs without electrical interference. Fiber segment L5 covered the area of the positive tab, the vent, and the negative tab. Thermocouples of TC1 and TC2 were also instrumented in the middle of the prismatic cell's front surface and rear surface, respectively.

Following the instrumentation of the optical fiber, position calibration was conducted with a heated plastic cube to identify the fiber segment attached on the cell surface, as shown in Table 1. It was essential to note the importance of meticulous data processing, considering both fiber deployment and position calibration. For instance, in the case of L2, the physical fiber segment started from a position of 3072 mm to 3223 mm, but the data process had to occur in reverse, from 3223 mm to 3072 mm, to correctly align with the fiber deployment of L1 and L3. TC1 and TC2 were positioned closely to the optical fiber sensor for calibration and performance comparison. The corresponding locations were 3151 mm for TC1 and 4781 mm for TC2 along the fiber length.

Table 1. Position calibration of the instrumented optical fiber sensors on the prismatic cell.

Fiber Segment	Start (mm)	End (mm)	Fiber Segment	Start (mm)	End (mm)
L1	2767	2923	L6	4165	4254
L2	3072	3223	L7	4416	4569
L3	3356	3496	L8	4712	4858
L4	3645	3755	L9	4986	5135
L5-positive	3886	3927			
L5-vent	3950	3978			
L5-negative	4001	4039			

The experimental setup of the prismatic cell with the distributed optical fiber sensor is shown in Figure 2c. The instrumented and calibrated prismatic cell was securely held in place by a bespoke designed jig and placed into a chamber (Binder-MKF56), which maintained a constant ambient temperature of 25 °C. Due to the 86 Ah capacity, a high-current cycler of Digatron MCT-RE was used as the battery management system for the cell charge and discharge. Thermocouple data were recorded by the Pico Logger. The optical fiber sensor was connected and demodulated by the OFDR interrogator. The measurement data, including voltage, current, Pico Logger, and OFDR interrogator data, were recorded at a frequency of 1 Hz.

The prismatic cell charge and discharge followed a conventional protocol: charge with constant current–constant voltage (CC–CV) and discharge with constant current (CC). During the CC–CV charge, the battery undergoes charging with a constant current until the voltage reached the limit of 4.2 V. Next, the voltage was maintained at 4.2 V with a gradually reducing current with a low limit current value of 15 A. The battery rested for 30 min between charge and discharge cycles. In the discharge phase, the battery was discharged with a constant current until it reached the lower limit of 2.8 V. Four sets of operation rates were investigated for the thermal analysis: (1) 0.3 C charge–0.3 C discharge, (2) 0.5 C charge–0.5 C discharge, (3) 1.0 C charge–1.0 C discharge, and (4) 1.5 C charge–1.5 C discharge.

3. Results

3.1. Spatial-Resolved Optical Measurements

Figure 3 represents the experimental measurements conducted during a 1.0 C CC–CV (constant current–constant voltage) charge and 1.0 C constant current (CC) discharge. There were two periods of charge/discharge with 86 A current.

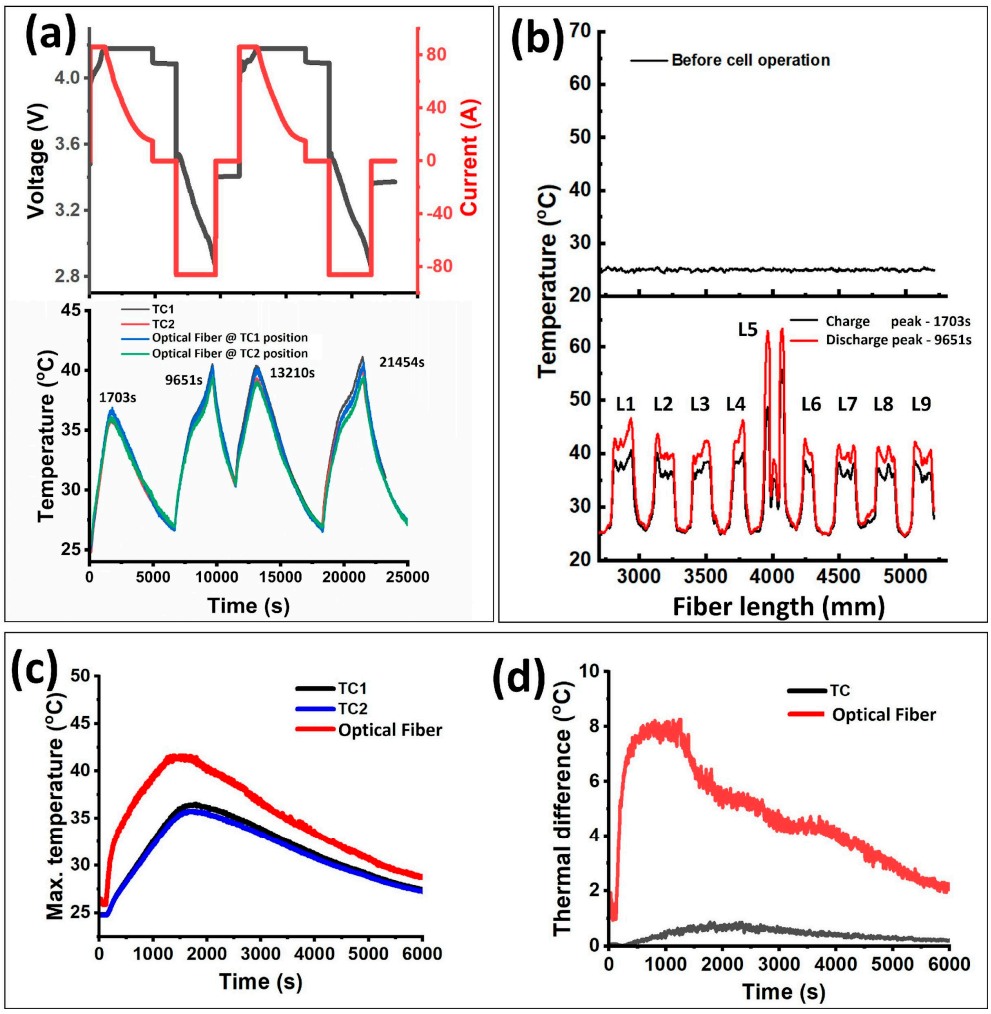

Figure 3. Spatial-resolved optical measurement and comparison with thermocouples. (**a**) Top—voltage and current under 1.0 C CC–CV charge and 1.0 C CC discharge; bottom—comparison between TC1 and optical fiber measurement. (**b**) Top—distributed optical measurement before cell operation; bottom—distributed optical measurement at 1703 s of the charge peak (black curve). Distributed optical measurement at 9651 s of the discharge peak (red curve). (**c**) Maximum temperature comparison between TC and the optical fiber under 1.0 C CC–CV charge. (**d**) Measured thermal difference comparison under 1.0 C CC–CV charge.

The surface thermal behavior was closely linked to the battery charge/discharge, as depicted in Figure 3a (bottom). Both the thermocouple and the optical fiber sensor could monitor heat generation and dissipation. TC1 and the corresponding point in the distributed optical fiber sensor (3151 mm) exhibited the same temperature profile during the 1.0 C charge/discharge, validating the performance of the distributed optical sensor. During the initial charge process, the maximum temperature was 36.7 °C at 1703 s. Most of the heat generation and accumulation happened during the CC charge phase. In the CV charge phase, the battery surface temperature gradually reduced to ambient levels. There was more heat generation during CC discharge. The peak temperature in the first discharge process was 40.3 °C at 9651 s.

In Figure 3b, the spatial temperature distribution at three specific time instances during the experiments is depicted. The initialized distributed optical measurement before the battery operation is shown in the top figure, which was around the ambient temperature of 25.0 °C. The black and red curves represent the distributed optical measurement of temperature peaks during charge and discharge, occurring at 1703 s and 9651 s, respectively.

Nine thermal peaks were observed along the fiber length, corresponding to nine optical fiber segments attached on the battery surface (Figure 2b). The result indicated that the temperature is not uniformly distributed along the optical fiber length, confirming the presence of thermal gradients within the prismatic cells. Furthermore, even within one single segment of fiber, such as L1, a temperature peak was observed at the end of L1, with a temperature of 46.7 °C. The maximum temperature difference within the L1 segment was already high at 5.9 °C.

The reason behind such thermal distribution and thermal gradient was explored further with the assistance of the global thermal image derived from the optical sensor. Additionally, the abnormal temperature peak during the L5 segment in Figure 3b was not neglected. The peak temperature of L5 reached 63.4 °C, approximately 20 degrees higher than the surface average temperature. It can be predicted that the current tabs play essential roles in prismatic cell thermal generation and dissipation.

The distributed optical sensor was compared to the instrumented thermocouples of TC1 and TC2 in Figures 3c,d. The optical measurement of the thermal gradient was derived from the maximum and minimum values of the segments L1-L9, with segment L5 excluded for the battery surface characterization. During the 1.0 C CC–CV charge process, the maximum temperature observed with the optical sensor was 41.6 °C, while the maximum values of TC1 and TC2 were 36.4 °C and 35.7 °C, respectively. The maximum temperature difference of the optical sensor could reach up to 8.2 °C, while the temperature difference between the two thermocouples was only 0.8 °C. This highlights that a conventional point-like characterization method needs extra thermal gradient investigation for sensor location [44].

3.2. Thermal Gradient Characterization with an Optical Fiber Sensor

Further 0.3 C, 0.5 C, and 1.5 C charge/discharge was investigated to demonstrate the performance of the optical fiber sensor in Figure 4. The current values for 0.3 C, 0.5 C, and 1.5 C were 25.8 A, 43.0 A, and 129.0 A, respectively. As the operation C-rate increased, more heat generation and thermal gradient were predicted and observed. The maximum temperature of the prismatic cell was 46.9 °C during 1.5 C charge, while the 1.5 C discharge process generated a peak temperature of 52.1 °C. During the charge process, the constant current (CC) stage dominated the thermal generation. In the discharge, the maximum temperature exponentially increased at the beginning of the discharge event. Toward the end of the discharge, there was another temperature rise before it reduced to the voltage limit. This temperature profile agrees with the behavior observed during battery open-circuit voltage (OCV) investigation [45,46]. It is noteworthy that even at constant voltage (CV), there is still battery thermal generation, because after the discharge temperature peak in Figure 4c, the temperature ought to have shown a steep decrease without any battery operation. But the moderate temperature decrease in the CV charge indicated the presence of thermal generation. The temperature decrease is mainly attributed to excessive heat dissipation.

Figure 4b,d show the thermal difference derived from the distributed optical fiber sensor. The maximum temperature difference during the 1.5 C charge was 12.9 °C, while the maximum temperature difference of 1.5 C discharge was 11.9 °C. Even at the lowest rate of 0.3 C, the measured temperature difference could reach up to 4.0 °C during battery charge and 3.8 °C during battery discharge. It was interesting to find that after the fast formation of the thermal gradient at the beginning of charge/discharge, there was a relatively stable stage of thermal difference. For example, in the case of the 1.5 C discharge in Figure 4d, the thermal gradient reached 10.3 °C just at 234 s, and then it stabilized around 11 °C during the rest of the CC process. A similar stable stage was observed during

the battery discharge. This indicates the existence of a certain thermal behavior during battery operation. However, the maximum temperature difference is only indictive of specific points (hottest and coolest) on the battery surface and cannot reveal more detailed information about the thermal distribution.

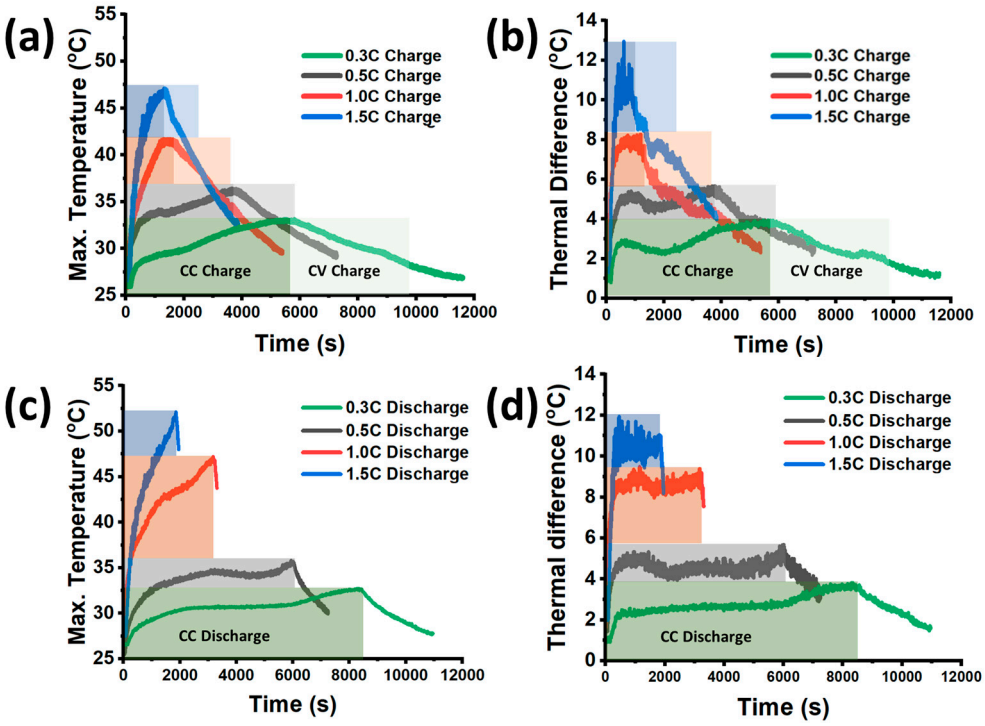

Figure 4. (**a**) Battery surface maximum temperature during the charge process. (**b**) Maximum thermal difference during the charge process. (**c**) Battery surface maximum temperature during the discharge process. (**d**) Maximum thermal difference during the battery discharge process.

Conventional monitoring methods, such as identifying the hottest spot [47,48] and the maximum thermal difference [49,50], are insufficient to fully understand the thermal behavior of prismatic cells. These methods are unable to capture the intricate details of heat generation and dissipation, which are crucial for battery investigation, modeling, and thermal management. Here, with optical distributed measurement, both the number of sensor locations and the resolution were significantly enhanced, allowing for expanded thermal analysis into the spatially resolved domain without increasing complexity.

The temperature variation along the instrumented optical fiber is illustrated in Figure 3b. Taking segments L1, L2, and L3 as examples, each segment exhibited its own temperature peak at the specific position, indicating the presence of distinct hot spots during discharge. Through the combination of position calibration outlined in Section 2, the distributed measurement along the fiber length was mapped to the practical fiber deployment on the battery surface. The spatial temperature distribution of the battery front surface is represented in Figure 5. Three segments of the optical fiber corresponded to the top-L1, middle-L2, and bottom-L3 horizontal measurements along the prismatic cell. The combined fiber length of these three segments was 447 mm, resulting in a total of 149 measurement locations under 3 mm resolution.

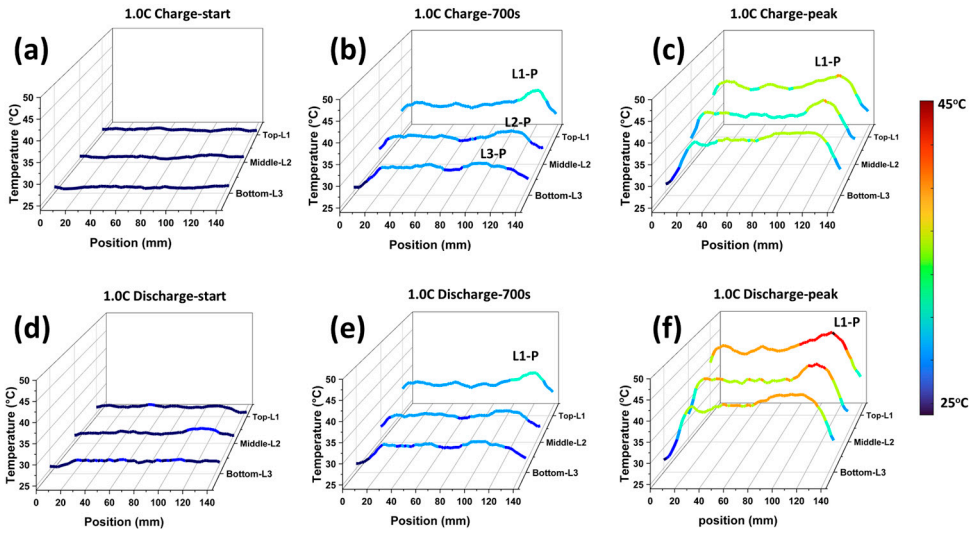

Figure 5. Spatial temperature distribution on the front surface of prismatic cells—mapped to Figure 2b (left). (**a**) Measurement before the cell operation. (**b**) Optical measurement at the early stage of the 1.0 C charge at 700 s. (**c**) Optical measurement at the time of the 1.0 C charge temperature peak. (**d**) Measurement before the 1.0 C discharge, after 30 min cooling down in the chamber after the 1.0 C battery charge. (**e**) Optical measurement at the early stage of the 1.0 C discharge at 700 s. (**f**) Optical measurement at the time of the 1.0 C discharge temperature peak.

Before cell operation, the surface temperature was uniform and approximately at ambient temperature, as shown in Figure 5a. After 700 s of 1.0 C CC charge, rapid heat generation was observed. Figure 5b illustrates that the temperature was not uniform across the cell surface. The L1 segment on the top exhibited an average temperature of 33.1 °C, higher than that of the middle 30.8 °C and the bottom 30.2 °C. Additionally, a peak temperature of 35.8 °C (L1-P) was detected on the top right of the battery surface, near the positive tabs. The interesting part is that similar temperature peaks were observed in the right portions of segments L2 (L2-P) and L3 (L3-P). However, the peak temperature gradually decreased to 31.9 °C (L2-P) and 31.5 °C (L3-P). The corresponding hottest locations were just below L1-P. To quantify the thermal difference among the surface temperatures, the coefficient of the thermal gradient (CTG) is defined as follows:

$$CTG = \frac{T_{max} - T_{min}}{T_{max}} \times 100\% \quad (3)$$

Therefore, at the start stage of the 1.0 C charge, the value of the CTG increased to 12.0%. Toward the end of the CC charge in Figure 5c, the average temperatures of L1, L2, and L3 rose to 37.7 °C, 36.5 °C, and 36.2 °C, respectively. The peak temperature on the right side still existed, with L1-P reaching 40.2 °C. However, despite the rise in average temperature, the thermal gradient did not increase proportionally. The CTG value was reduced to 4.4%, as shown in Figure 5c, indicating a more uniform thermal distribution than that in Figure 5b.

A similar trend was observed during the 1.0 C CC discharge process in Figure 5d–f. The top-right hottest spot was observed at the beginning stage of discharge. The peak temperature of L1-P was 37.9 °C, and the CTG was 12.4%. As the discharge progressed, the average temperature continuously increased. By the end of the discharge (Figure 5f), the peak temperature of L1-P was 46.1 °C. It was noted that the thermal gradient was enhanced, with a CTG value of 7.2%.

In addition to the hottest spot on the top right during both charge and discharge, the fiber segment on the top left also experienced higher thermal generation compared

to most parts of the cell surface. At the end of both 1.0 C charge and 1.0 C discharge in Figures 5c,f, the peak temperature on the top left reached 38.9 °C and 42.9 °C, respectively. Two peaks, one on the left and one on the right, create a valley profile in the middle of the L1 segment. Furthermore, similar temperature valley profiles are also observed in the segments of middle-L2 and bottom-L3.

4. Discussion

4.1. Heat Generation on Current Tabs

Here, we can recall the temperature distribution profile in Figure 3b, where the locations of the tabs experience abnormally higher temperatures than other parts. To further explore the thermal generation of prismatic cells, tab temperatures were recorded and compared to the hottest surface spot in Figure 6 and Table 2. Results showed that the current tabs always experience more heat generation compared to the surface. During the 0.3 C CC–CV charge in Figure 6a, the negative tab reached a peak temperature of 39.4 °C, and the positive tab reached a peak temperature of 34.5 °C. Both temperatures were higher than the surface maximum temperature of 33.1 °C, which is also near the current tabs. The temperature difference increased with a higher charge/discharge rate. Under the 1.0 C CC–CV charge, the negative tab and the positive tab had a peak temperature of 68.1 °C and 58.0 °C, respectively, which is more than 20 degrees higher than the surface temperature of 41.6 °C. With a 1.5 C CC–CV charge, the temperature of the negative tab further increased to 102.7 °C, which poses a considerable risk to normal battery operation [51,52]. The same temperature behavior occurred during the CC discharge process in Figure 6b, where the peak temperature of the negative tab reached 113.9 °C with a 1.5 C discharge rate.

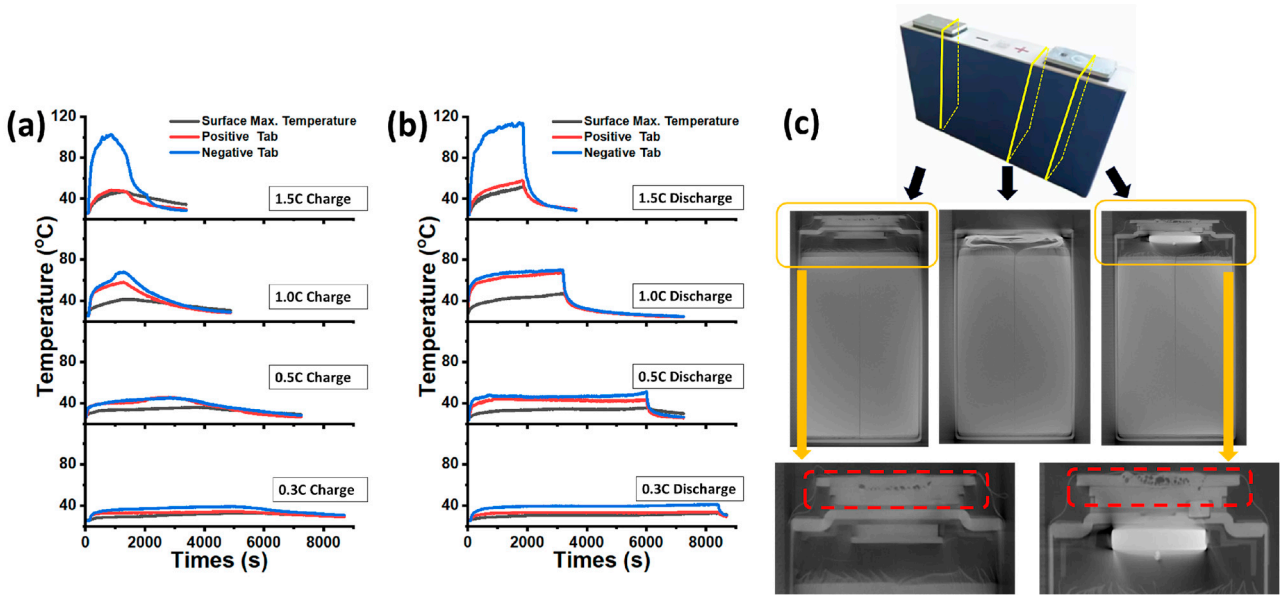

Figure 6. (**a**) Temperature comparison between the cell surface's hottest spot and positive and negative tabs under various charge rates. (**b**) Temperature comparison under various discharge rates. (**c**) CT scan images of the battery's vertical cross section. Left—negative tab; middle—intermediary section; right—positive tabs.

Table 2. Temperature measurement including current tabs and the surface's hottest spot.

C-Rate	Charge/Discharge	Positive Tab (°C)	Negative Tab (°C)	Surface Maximum (°C)
0.3	Charge	34.5	39.4	33.1
	Discharge	34.1	41.0	32.7
0.5	Charge	45.4	45.5	36.3
	Discharge	43.3	51.2	35.7
1.0	Charge	58.0	68.1	41.6
	Discharge	67.4	70.2	47.2
1.5	Charge	48.7	102.7	46.9
	Discharge	57.7	113.9	52.1

Figure 6c illustrates the CT scans of prismatic cells. Inside the battery can, the layers of electrode and separator were uniformly folded. Multiple current collectors were welded to stacks of metals to form the external current tab/terminal. A CT scan revealed a complex tab structure and imperfect metal welding, as shown at the bottom of Figure 6c (dashed red line). This observation suggests that extra thermal generation may occur when many electrons gather on the tabs during high-rate operation [53–55]. It was noted that the measured direct current internal resistance (DC-IR) was 0.6 mohm, still within the datasheet of 0.8 mohm.

An intriguing observation was the disparity in thermal behavior between the tabs under 1.5 C charge/discharge conditions. While the negative tab experienced increasing thermal generation up to 113.9 °C, the temperature on the positive tab does not significantly increase as expected under a 1.5 C charge/discharge. In fact, it is even lower than the peak temperature observed at 1.0 C charge/discharge. This abnormal phenomenon could be attributed to side-effect reactions occurring inside the battery due to the high-rate operation [56]. The tab position and dimension play dominant roles in thermal gradient formation, because the tabs are usually not specifically designed in a uniform/symmetric profile, while the electrode and the separator are uniformly folded. The 21,700 cells' non-uniform tabs generate a thermal gradient along the circumference direction [44].

4.2. Operando Global Thermal Image

All the analyses mentioned so far were based on either the time domain or the spatial domain, which cannot fully reveal the capability of a distributed optical fiber sensor. Therefore, we presented the operando thermal image of the prismatic cell in Figure 7. It comprised one 1.0 C CC–CV charge and one 1.0 C CC discharge in the time domain. In the spatial domain, it included four cell surfaces, a positive tab, a vent, and a negative tab. The operando thermal image can be investigated and understood as follows:

(1) During the start of charge/discharge, heat is rapidly generated and accumulated primarily on current tabs, while the prismatic cell surfaces maintain a relatively lower temperature (Figure 7a).

(2) The temperature in the vicinity of the positive/negative tabs begins to rise compared to the rest of the surface (Figure 7b). Notably, hot spots emerge on the top right in the front view, the top left in the rear view, and the top in the Side-P and Side-N views.

(3) As the charge/discharge progresses, the heat is transmitted to the other parts of the surface, although not uniformly like a point/line source. Instead, thermal accumulation is observed around the areas beneath the current tabs (Figure 7c).

(4) Following the completion of charge/discharge, the heat gradually dissipates and is transmitted downward to the bottom of the battery (Figure 7d).

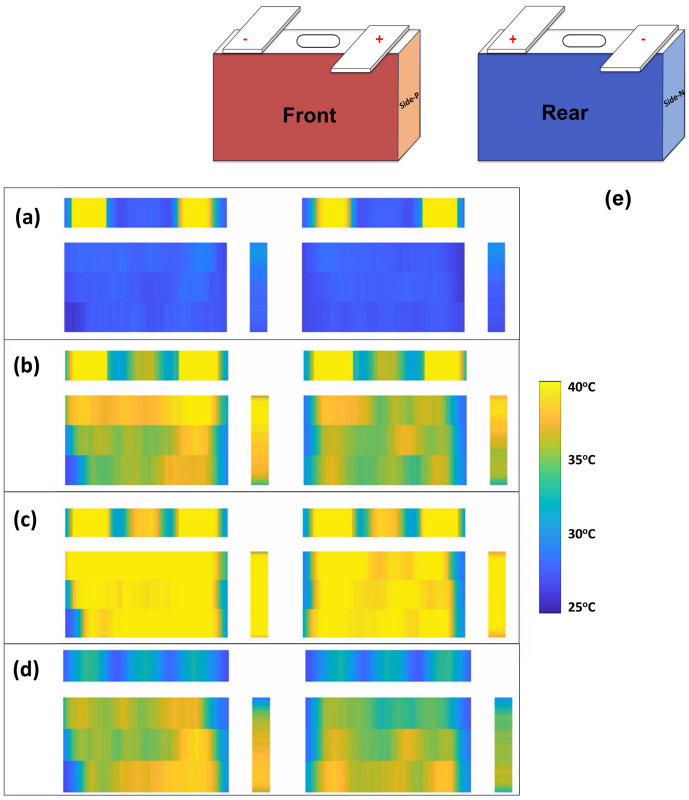

Figure 7. Thermal image with the optical fiber sensor. (**a**) Tabs' thermal generation at the start of the 1.0 C CC discharge. (**b**) Hotspot generation on the battery surface. (**c**) Battery surface thermal distribution at the temperature peak of 1.0 C discharge. (**d**) Thermal dissipation after the CC discharge. (**e**) Video of the operando thermal image of the prismatic cell under a 1.0 C CC–CV charge and a 1.0 C CC discharge.

It is reasonable to assume that the heat is rapidly generated and readily accumulated at the prismatic cell tabs before being transmitted to the cell surface and bottom. This assumption can be validated by optical measurements on the left and right sides of the prismatic cells (Side-P and Side-N in Figure 7). It means that the electric-resistance-induced thermal energy, such as at the tab structure and the welding point, dominates the internal chemics-electric thermal behavior under the rapid battery charge/discharge cycles. This insight provides a deeper understanding of thermal behavior in the large-format prismatic cell. Moreover, despite the negative tab experiencing a higher peak temperature (Figure 6), the positive tab appears to play a more active role in the thermal transmission and dissipation. Following the charge/discharge, residual heat tends to accumulate predominately on the bottom right of the cell, below the position of the positive tab. This phenomenon may be influenced by various factors, including battery materials and structures (such as tabs, electrodes, and jellyroll folding), jig design, and the airflow pattern within the chamber.

5. Conclusions

In summary, this study achieved an operando thermal image covering the entire surface of a prismatic cell using a distributed optical fiber sensor, allowing for detailed characterization of hotspot generation and the thermal gradient. The proposed optical sensor, based on the Rayleigh scattering optical frequency domain reflectometer, simplifies the cell instrumentation process without compromising sensing performance. With a spatial resolution of 3 mm achieved using a tunable laser source and the suppression of nonlinear sweep noise, the sensor enables superior monitoring of hotspot generation and analysis of the thermal gradient compared to conventional point-like thermocouples. Direct

attachment of the optical fiber sensor to the metal tabs reveals the essential role of current tabs during battery operation. Results show that during a rapid charge/discharge operation, heat is more readily generated and accumulated on tabs than on the battery surface, while the heat is likely to dissipate on the side of the positive current tab. This detailed thermal characterization aids in further exploration of the fundamental mechanisms of batteries and expands the research boundaries of cell design, thermal management, and battery modeling. Moreover, the distributed optical fiber sensor can be transferred to the module/pack, where the thermal gradient is more severe for the battery management systems. By delivering a detailed thermal distribution with millimeter-level resolution and eliminating the need for massive cell instrumentation and wire connections of point-like sensors, the distributed optical fiber sensor presents itself as a potential technique for future battery and energy applications.

Further study should focus on decoupling the optical fiber's cross-sensitivity between the temperature and strain to expand the optical measurement capability. The price of an OFDR interrogator also needs to be reduced for the battery/energy application. The expensive tunable laser source can be potentially replaced by a narrow-linewidth laser with external modulation.

Author Contributions: Conceptualization, Z.G. and M.A.V.; methodology, Z.G. and M.A.V.; software, C.B.; validation, Z.G. and C.B.; formal analysis, Z.G. and E.G.; investigation, Z.G.; resources, C.B.; data curation, Z.G.; writing—original draft preparation, Z.G. and M.A.V.; writing—review and editing, J.M.; visualization, Z.G.; supervision, J.M.; project administration, Z.G.; funding acquisition, Z.G. and M.A.V. All authors have read and agreed to the published version of the manuscript.

Funding: This work was funded by Jaguar Land Rover Catapult (JLRC 9238).

Data Availability Statement: The data that support the findings of this study are available from the corresponding author upon request.

Acknowledgments: The authors would like to thank Iain Masters for the CT scan and Harry Evans and Jason Page for project management.

Conflicts of Interest: Author Mina Abedi Varnosfaderani was employed by the company Jaguar Land Rover. The remaining authors declare that the research was conducted in the absence of any commercial or financial relationships that could be construed as a potential conflict of interest. The authors declare that this study received funding from Jaguar Land Rover Catapult. The funder was not involved in the study design, collection, analysis, interpretation of data, the writing of this article or the decision to submit it for publication.

References

1. Liu, K.; Liu, Y.; Lin, D.; Pei, A.; Cui, Y. Materials for lithium-ion battery safety. *Sci. Adv.* **2018**, *4*, eaas9820. [CrossRef] [PubMed]
2. Sun, P.; Bisschop, R.; Niu, H.; Huang, X. A review of battery fires in electric vehicles. *Fire Technol.* **2020**, *56*, 1361–1410. [CrossRef]
3. Victor Chombo, P.; Laoonual, Y.; Wongwises, S. Lessons from the electric vehicle crashworthiness leading to battery fire. *Energies* **2021**, *14*, 4802. [CrossRef]
4. Kolly, J.M.; Panagiotou, J.; Czech, B.A. *The Investigation of a Lithium-Ion Battery Fire Onboard a Boeing 787 by the US National Transportation Safety Board*; Safety Research Corporation of America: Dothan, AL, USA, 2013; pp. 1–18.
5. Williard, N.; He, W.; Hendricks, C.; Pecht, M. Lessons learned from the 787 dreamliner issue on lithium-ion battery reliability. *Energies* **2013**, *6*, 4682–4695. [CrossRef]
6. Mankowski, P.J.; Kanevsky, J.; Bakirtzian, P.; Cugno, S. Cellular phone collateral damage: A review of burns associated with lithium battery powered mobile devices. *Burns* **2016**, *42*, e61–e64. [CrossRef] [PubMed]
7. Loveridge, M.J.; Remy, G.; Kourra, N.; Genieser, R.; Barai, A.; Lain, M.J.; Guo, Y.; Amor-Segan, M.; Williams, M.A.; Amietszajew, T.; et al. Looking deeper into the Galaxy (Note 7). *Batteries* **2018**, *4*, 3. [CrossRef]
8. Zhu, G.; Wen, K.; Lv, W.; Zhou, X.; Liang, Y.; Yang, F.; Chen, Z.; Zou, M.; Li, J.; Zhang, Y.; et al. Materials insights into low-temperature performances of lithium-ion batteries. *J. Power Sources* **2015**, *300*, 29–40. [CrossRef]

9. Waqas, M.; Ali, S.; Feng, C.; Chen, D.; Han, J.; He, W. Recent development in separators for high-temperature lithium-ion batteries. *Small* **2019**, *15*, 1901689. [CrossRef]
10. Pan, J.; Li, H.; Sun, H.; Zhang, Y.; Wang, L.; Liao, M.; Sun, X.; Peng, H. A lithium–air battery stably working at high temperature with high rate performance. *Small* **2018**, *14*, 1703454. [CrossRef]
11. Lin, J.; Liu, X.; Li, S.; Zhang, C.; Yang, S. A review on recent progress, challenges and perspective of battery thermal management system. *Int. J. Heat Mass Transf.* **2021**, *167*, 120834. [CrossRef]
12. Xia, G.; Cao, L.; Bi, G. A review on battery thermal management in electric vehicle application. *J. Power Sources* **2017**, *367*, 90–105. [CrossRef]
13. Hémery, C.V.; Pra, F.; Robin, J.F.; Marty, P. Experimental performances of a battery thermal management system using a phase change material. *J. Power Sources* **2014**, *270*, 349–358. [CrossRef]
14. Jiang, Z.Y.; Qu, Z.G. Lithium–ion battery thermal management using heat pipe and phase change material during discharge–charge cycle: A comprehensive numerical study. *Appl. Energy* **2019**, *242*, 378–392. [CrossRef]
15. Pesaran, A.A. Battery thermal models for hybrid vehicle simulations. *J. Power Sources* **2002**, *110*, 377–382. [CrossRef]
16. Werner, D.; Paarmann, S.; Wiebelt, A.; Wetzel, T. Inhomogeneous temperature distribution affecting the cyclic aging of Li-ion cells. Part I: Experimental investigation. *Batteries* **2020**, *6*, 13. [CrossRef]
17. Zhang, G.; Cao, L.; Ge, S.; Wang, C.Y.; Shaffer, C.E.; Rahn, C.D. In situ measurement of radial temperature distributions in cylindrical Li-ion cells. *J. Electrochem. Soc.* **2014**, *161*, A1499. [CrossRef]
18. Hunt, I.A.; Zhao, Y.; Patel, Y.; Offer, G.J. Surface cooling causes accelerated degradation compared to tab cooling for lithium-ion pouch cells. *J. Electrochem. Soc.* **2016**, *163*, A1846. [CrossRef]
19. Yu, Y.; Vergori, E.; Worwood, D.; Tripathy, Y.; Guo, Y.; Somá, A.; Greenwood, D.; Marco, J. Distributed thermal monitoring of lithium-ion batteries with optical fiber sensors. *J. Energy Storage* **2021**, *39*, 102560. [CrossRef]
20. Vincent, T.A.; Gulsoy, B.; Sansom, J.E.; Marco, J. In-situ instrumentation of cells and power line communication data acquisition towards smart cell development. *J. Energy Storage* **2022**, *50*, 104218. [CrossRef]
21. Li, R.; Li, W.; Singh, A.; Ren, D.; Hou, Z.; Ouyang, M. Effect of external pressure and internal stress on battery performance and lifespan. *Energy Storage Mater.* **2022**, *52*, 395–429. [CrossRef]
22. Lu, P.; Lalam, N.; Badar, M.; Liu, B.; Chorpening, B.T.; Buric, M.P.; Ohodnicki, P.R. Distributed optical fiber sensing: Review and perspective. *Appl. Phys. Rev.* **2019**, *6*, 041302. [CrossRef]
23. Yan, Y.; Zheng, H.; Zhao, Z.; Guo, C.; Wu, X.; Hu, J.; Lau, A.P.T.; Lu, C. Distributed optical fiber sensing assisted by optical communication techniques. *J. Light. Technol.* **2021**, *39*, 3654–3670. [CrossRef]
24. Ding, Z.; Wang, C.; Liu, K.; Jiang, J.; Yang, D.; Pan, G.; Pu, Z.; Liu, T. Distributed optical fiber sensors based on optical frequency domain reflectometry: A review. *Sensors* **2018**, *18*, 1072. [CrossRef]
25. Islam, M.R.; Ali, M.M.; Lai, M.H.; Lim, K.S.; Ahmad, H. Chronology of Fabry-Perot interferometer fiber-optic sensors and their applications: A review. *Sensors* **2014**, *14*, 7451–7488. [CrossRef]
26. Pan, R.; Yang, W.; Li, L.; Yang, Y.; Zhang, L.; Yu, X.; Fan, J.; Yu, S.; Xiong, Y. A high-sensitive fiber-optic Fabry-Perot sensor with parallel polymer-air cavities based on vernier effect for simultaneous measurement of pressure and temperature. *IEEE Sens. J.* **2021**, *21*, 21577–21585. [CrossRef]
27. Zhao, Y.; Zhao, J.; Peng, Y.; Tong, R.J.; Cai, L. Simultaneous measurement of seawater salinity and temperature with composite fiber-optic interferometer. *IEEE Trans. Instrum. Meas.* **2021**, *71*, 1–8. [CrossRef]
28. Dong, Y.; Hu, P.; Ran, M.; Fu, H.; Yang, H.; Yang, R. Correction of nonlinear errors from PGC carrier phase delay and AOIM in fiber-optic interferometers for nanoscale displacement measurement. *Opt. Express* **2020**, *28*, 2611–2624. [CrossRef]
29. Zhang, H.; Ye, W.; Wei, C.; Xia, Y.; Chang, S.; Liao, Z.; Hu, L. Improved phase sensitivity in a quantum optical interferometer based on multiphoton catalytic two-mode squeezed vacuum states. *Phys. Rev. A* **2021**, *103*, 013705. [CrossRef]
30. Ee, Y.J.; Tey, K.S.; Lim, K.S.; Shrivastava, P.; Adnan, S.B.R.S.; Ahmad, H. Lithium-ion battery state of charge (SoC) estimation with non-electrical parameter using uniform fiber Bragg grating (FBG). *J. Energy Storage* **2021**, *40*, 102704. [CrossRef]
31. Mei, W.; Liu, Z.; Wang, C.; Wu, C.; Liu, Y.; Liu, P.; Xia, X.; Xue, X.; Han, X.; Sun, J.; et al. Operando monitoring of thermal runaway in commercial lithium-ion cells via advanced lab-on-fiber technologies. *Nat. Commun.* **2023**, *14*, 5251. [CrossRef]
32. Peng, J.; Jia, S.; Yu, H.; Kang, X.; Yang, S.; Xu, S. Design and experiment of FBG sensors for temperature monitoring on external electrode of lithium-ion batteries. *IEEE Sens. J.* **2020**, *21*, 4628–4634. [CrossRef]
33. Zhou, L.; Wang, F.; Wang, X.; Pan, Y.; Sun, Z.; Hua, J.; Zhang, X. Distributed strain and vibration sensing system based on phase-sensitive OTDR. *IEEE Photonics Technol. Lett.* **2015**, *27*, 1884–1887. [CrossRef]
34. Tomboza, W.; Guerrier, S.; Awwad, E.; Dorize, C. High sensitivity differential phase OTDR for acoustic signals detection. *IEEE Photonics Technol. Lett.* **2021**, *33*, 645–648. [CrossRef]
35. Zinsou, R.; Liu, X.; Wang, Y.; Zhang, J.; Wang, Y.; Jin, B. Recent progress in the performance enhancement of phase-sensitive OTDR vibration sensing systems. *Sensors* **2019**, *19*, 1709. [CrossRef]

36. Passy, R.; Gisin, N.; von der Weid, J.P.; Gilgen, H.H. Experimental and theoretical investigations of coherent OFDR with semiconductor laser sources. *J. Light. Technol.* **1994**, *12*, 1622–1630. [CrossRef]
37. Ito, F.; Fan, X.; Koshikiya, Y. Long-range coherent OFDR with light source phase noise compensation. *J. Light. Technol.* **2011**, *30*, 1015–1024. [CrossRef]
38. Guo, Z.; Han, G.; Yan, J.; Greenwood, D.; Marco, J.; Yu, Y. Ultimate spatial resolution realisation in optical frequency domain reflectometry with equal frequency resampling. *Sensors* **2021**, *21*, 4632. [CrossRef]
39. Guo, Z.; Yan, J.; Han, G.; Greenwood, D.; Marco, J.; Yu, Y. High sensing accuracy realisation with millimetre/sub-millimetre resolution in optical frequency domain reflectometer. *J. Light. Technol.* **2022**, *40*, 4050–4056. [CrossRef]
40. Guo, Z.; Yan, J.; Han, G.; Yu, Y.; Greenwood, D.; Marco, J. High-resolution ϕ-OFDR using phase unwrap and nonlinearity suppression. *J. Light. Technol.* **2023**, *41*, 2885–2891.
41. Han, G.; Yan, J.; Guo, Z.; Greenwood, D.; Marco, J.; Yu, Y. A review on various optical fiber sensing methods for batteries. *Renew. Sustain. Energy Rev.* **2021**, *150*, 111514. [CrossRef]
42. Jones, J.D. Review of fiber sensor techniques for temperature-strain discrimination. In Proceedings of the 12th International Conference on Optical Fiber Sensors, Williamsburg, VA, USA, 28–31 October 1997; Optica Publishing Group: Washington, DC, USA, 1997; p. OTuC1.
43. Wijaya, H.; Rajeev, P.; Gad, E. Distributed optical fiber sensor for infrastructure monitoring: Field applications. *Opt. Fiber Technol.* **2021**, *64*, 102577. [CrossRef]
44. Guo, Z.; Briggs, C.; Vincent, T.A.; Gulsoy, B.; Sansom, J.E.; Marco, J. Global thermal image of cylindrical 21700 Li-ion batteries with distributed optical fiber sensor. *J. Power Sources* **2024**, *592*, 233980. [CrossRef]
45. Mevawalla, A.; Panchal, S.; Tran, M.K.; Fowler, M.; Fraser, R. Mathematical heat transfer modelling and experimental validation of lithium-ion battery considering: Tab and surface temperature, separator, electrolyte resistance, anode-cathode irreversible and reversible heat. *Batteries* **2020**, *6*, 61. [CrossRef]
46. Zhang, L.; Fan, W.; Wang, Z.; Li, W.; Sauer, D.U. Battery heating for lithium-ion batteries based on multi-stage alternative currents. *J. Energy Storage* **2020**, *32*, 101885. [CrossRef]
47. Huang, Z.; Yu, Y.; Duan, Q.; Qin, P.; Sun, J.; Wang, Q. Heating position effect on internal thermal runaway propagation in large-format lithium iron phosphate battery. *Appl. Energy* **2022**, *325*, 119778. [CrossRef]
48. Choudhari, V.G.; Dhoble, A.S.; Sathe, T.M. A review on effect of heat generation and various thermal management systems for lithium ion battery used for electric vehicle. *J. Energy Storage* **2020**, *32*, 101729. [CrossRef]
49. Fear, C.; Parmananda, M.; Kabra, V.; Carter, R.; Love, C.T.; Mukherjee, P.P. Mechanistic underpinnings of thermal gradient induced inhomogeneity in lithium plating. *Energy Storage Mater.* **2021**, *35*, 500–511. [CrossRef]
50. Carter, R.; Kingston, T.A.; Atkinson, R.W.; Parmananda, M.; Dubarry, M.; Fear, C.; Mukherjee, P.P.; Love, C.T. Directionality of thermal gradients in lithium-ion batteries dictates diverging degradation modes. *Cell Rep. Phys. Sci.* **2021**, *2*, 100351. [CrossRef]
51. Lin, X.; Zhou, G.; Liu, J.; Yu, J.; Effat, M.B.; Wu, J.; Ciucci, F. Rechargeable battery electrolytes capable of operating over wide temperature windows and delivering high safety. *Adv. Energy Mater.* **2020**, *10*, 2001235. [CrossRef]
52. Chen, Y.; Kang, Y.; Zhao, Y.; Wang, L.; Liu, J.; Li, Y.; Liang, Z.; He, X.; Li, X.; Tavajohi, N.; et al. A review of lithium-ion battery safety concerns: The issues, strategies, and testing standards. *J. Energy Chem.* **2021**, *59*, 83–99. [CrossRef]
53. Mei, W.; Chen, H.; Sun, J.; Wang, Q. Numerical study on tab dimension optimization of lithium-ion battery from the thermal safety perspective. *Appl. Therm. Eng.* **2018**, *142*, 148–165. [CrossRef]
54. Lyu, P.; Liu, X.; Liu, C.; Rao, Z. Experimental and modeling investigation on thermal risk evaluation of tabs for pouch-type lithium-ion battery and the relevant heat rejection strategies. *Int. J. Heat Mass Transf.* **2023**, *202*, 123770. [CrossRef]
55. Zeng, Y.; Chalise, D.; Lubner, S.D.; Kaur, S.; Prasher, R.S. A review of thermal physics and management inside lithium-ion batteries for high energy density and fast charging. *Energy Storage Mater.* **2021**, *41*, 264–288. [CrossRef]
56. Feng, X.; Ouyang, M.; Liu, X.; Lu, L.; Xia, Y.; He, X. Thermal runaway mechanism of lithium ion battery for electric vehicles: A review. *Energy Storage Mater.* **2018**, *10*, 246–267. [CrossRef]

Disclaimer/Publisher's Note: The statements, opinions and data contained in all publications are solely those of the individual author(s) and contributor(s) and not of MDPI and/or the editor(s). MDPI and/or the editor(s) disclaim responsibility for any injury to people or property resulting from any ideas, methods, instructions or products referred to in the content.